

Air-Stable 2D Cr₅Te₈ Nanosheets with Thickness-Tunable Ferromagnetism

Chao Chen, Xiaodie Chen, Changwei Wu, Xiao Wang,* Yue Ping, Xin Wei, Xing Zhou, Jiangbo Lu, Lujun Zhu, Jiadong Zhou, Tianyou Zhai, Junbo Han,* and Hua Xu*

2D magnetic materials have aroused widespread research interest owing to their promising application in spintronic devices. However, exploring new kinds of 2D magnetic materials with better stability and realizing their batch synthesis remain challenging. Herein, the synthesis of air-stable 2D Cr₅Te₈ ultrathin crystals with tunable thickness via tube-in-tube chemical vapor deposition (CVD) growth technology is reported. The importance of tube-in-tube CVD growth, which can significantly suppress the equilibrium shift to the decomposition direction and facilitate that to the synthesis reaction direction, for the synthesis of high-quality Cr₅Te₈ with accurate composition, is highlighted. By precisely adjusting the growth temperature, the thickness of Cr₅Te₈ nanosheets is tuned from ≈ 1.2 nm to tens of nanometers, with the morphology changing from triangles to hexagons. Furthermore, magneto-optical Kerr effect measurements reveal that the Cr₅Te₈ nanosheet is ferromagnetic with strong out-of-plane spin polarization. The Curie temperature exhibits a monotonic increase from 100 to 160 K as the Cr₅Te₈ thickness increases from 10 to 30 nm and no apparent variation in surface roughness or magnetic properties after months of exposure to air. This study provides a robust method for the controllable synthesis of high-quality 2D ferromagnetic materials, which will facilitate research progress in spintronics.

1. Introduction

2D materials have attracted considerable interest owing to their abundant structures and remarkable properties for fundamental study and potential technological applications.^[1–4] In recent years, the discovery of 2D ferromagnets has also provided an ideal platform for exploring and understanding magnetism in the ultimate 2D limit,^[5–9] for example, the critical behavior and dimensional cross-over of magnetic ordering.^[10,11] To date, several 2D magnetic materials with fascinating magnetic properties have been sequentially explored.^[12–14] For instance, layer-dependent ferromagnetism with out-of-plane anisotropy was observed in CrI₃ and Cr₂Ge₂Te₆ flakes at low temperatures.^[11,14] Bilayer CrI₃ even presented electrically tunable magnetic order, which can be reversibly switched between antiferromagnetism and ferromagnetism.^[15] Furthermore, gate-tunable room-temperature ferromagnetism was induced in four-layer

C. Chen, Y. Ping, X. Wei, H. Xu
 Key Laboratory of Applied Surface and Colloid Chemistry
 (Ministry of Education)
 Shaanxi Key Laboratory for Advanced Energy Devices
 School of Materials Science and Engineering
 Shaanxi Normal University
 Xi'an 710119, P. R. China
 E-mail: xuhua-nano@snnu.edu.cn

X. D. Chen, J. B. Han
 Wuhan National High Magnetic Field Centre
 Department of Physics
 Huazhong University of Science and Technology
 Wuhan 430074, P. R. China
 E-mail: junbo.han@mail.hust.edu.cn

C. W. Wu, X. Wang
 Shenzhen Key Laboratory of Nanobiomechanics
 Shenzhen Institutes of Advanced Technology
 Chinese Academy of Sciences
 Shenzhen, Guangdong 518055, P. R. China
 E-mail: xiao.wang@siat.ac.cn

X. Zhou, T. Y. Zhai
 State Key Laboratory of Material Processing and Die
 & Mould Technology
 School of Materials Science and Engineering
 Huazhong University of Science and Technology
 Wuhan 430074, P. R. China

J. B. Lu, J. L. Zhu
 School of Physics and Information Technology
 Shaanxi Normal University
 Xi'an 710119, P. R. China

J. D. Zhou
 Key Lab of Advanced Optoelectronic Quantum Architecture
 and Measurement (Ministry of Education)
 School of Physics
 Beijing Institute of Technology
 Beijing 100081, P. R. China



The ORCID identification number(s) for the author(s) of this article can be found under <https://doi.org/10.1002/adma.202107512>.

DOI: 10.1002/adma.202107512

Fe_3GeTe_2 flakes by an ionic gating method.^[16] Hence, 2D ferromagnets provide exciting technological opportunities for magnetic sensing and information storage.^[7,8]

However, the choice of presently available 2D magnetic materials is still quite limited, and most of them suffer from instability in the ambient atmosphere,^[11,14] which inevitably hinders intrinsic magnetism explorations and practical applications.^[17] Moreover, the majority of recently investigated 2D magnetic materials were mainly achieved by the mechanical exfoliation route, which possesses poor controllability of the morphology, domain size, and thickness. Hence, exploring new kinds of 2D magnetic materials with better stability and developing facile and batch-producible synthetic routes to controllably prepare them are of considerable importance for further development of this field. Toward this end, several pioneering studies have synthesized ultrathin 2D magnetic materials, for example, layered (VSe_2 and CrSe_2) and nonlayered (such as FeTe , Cr_2S_3 , and CrSe), by using chemical vapor deposition (CVD) approach.^[18–25] As tellurium (Te) has very strong spin-orbit coupling,^[26,27] chromium telluride (Cr_xTe_y) should be more inclined to generate strong magnetic anisotropy for stabilizing the long-range magnetic order in 2D systems and would thus yield a high Curie temperature (T_C). More importantly, Cr_xTe_y contains a series of possible materials with different compositions and structures, such as CrTe_2 , Cr_5Te_8 , Cr_2Te_3 , Cr_3Te_4 , and CrTe ,^[28] which may bring great opportunities to explore the distinctive magnetic properties of these materials in the 2D limit. As expected, significant difference in the thickness-dependent magnetic order between CrTe_2 , Cr_2Te_3 , and CrTe have been revealed,^[29–31] while the magnetic properties of Cr_5Te_8 down to the 2D limit are still unexplored. Previous reports have demonstrated that bulk Cr_5Te_8 is an intrinsic ferromagnetic (FM) compound with a high T_C of about 230 K.^[32–34] It is predicted that 2D Cr_5Te_8 should possess large magnetocrystalline anisotropy.^[34] However, owing to the naturally nonlayered structure and thermally unstable features, controllable synthesis of atomically thin Cr_5Te_8 crystal with accurate composition and high crystallinity remains a big challenge.

In this work, we report the thickness-controlled synthesis of 2D Cr_5Te_8 nanosheets and the investigation of their thickness-dependent magnetic properties. A tube-in-tube CVD growth strategy was developed to ensure a Te-rich growth atmosphere, which is critical to the synthesis of high-crystallinity Cr_5Te_8 nanosheets. Extensive experimental characterizations combined with structural simulations confirmed the composition, phase structure, and high crystallinity of the as-grown Cr_5Te_8 nanosheets. By precisely tuning the growth temperature from 600 to 900 °C, the thickness of as-grown Cr_5Te_8 nanosheets was controllably modulated from 1.2 to 30 nm, with the morphology changing from triangle to hexagon. Furthermore, the magnetism was studied by the magneto-optical Kerr effect (MOKE) technique, and as the thickness varied from 30 to 10 nm, the hard magnetism was sustained quite well, with the T_C decreasing from 160 to 100 K. Theoretical calculations suggest that the strong interlayer coupling within Cr_5Te_8 plays a critical role in the magnetic order in thick Cr_5Te_8 nanosheets. Notably, the aging experiment of Cr_5Te_8 nanosheets in ambient air demonstrates their superior environmental stability.

2. Results and Discussion

To realize precise synthesis of ultrathin Cr_5Te_8 crystals with a high crystal quality, a tube-in-tube CVD growth strategy was used to ensure sufficient feeding of Cr and Te sources, as schematically shown in **Figure 1a** (top row). Briefly, a built-in quartz tube (diameter of 1.5 cm and length of 15 cm) with one side open and the other side semi-open (3 mm tiny hole) was placed in a 1 in. tube furnace to serve as the reaction system. Te and chromium dichloride (CrCl_2) powders were used as precursors and placed at the forepart and interior of the built-in tube, respectively. Fluorophlogopite mica ($\text{KMg}_3\text{AlSi}_3\text{O}_{10}\text{F}_2$) was selected as the growth substrate for synthesizing ultrathin Cr_5Te_8 nanosheets, considering its atomically flat surface and chemically inert nature. More details about the sample synthesis are described in the Experimental Section.

As shown in **Figure 1a** (bottom row), Cr_5Te_8 crystallizes in the hexagonal structure with a space group $\text{Pm}\bar{1}$.^[32] The Cr atoms are located at two crystallographically different sites, leading to the formation of a nonlayered structure of CdI_2 type. In this regard, the nonlayered Cr_5Te_8 crystal can be viewed as a self-intercalation compound of layered CrTe_2 , where the inner layer and the intercalated Cr atoms are defined as Cr_1 and Cr_2 , respectively. **Figure 1b** shows a typical optical microscopy (OM) image of the as-grown Cr_5Te_8 nanosheets on mica substrate. We can see that some regular triangular Cr_5Te_8 nanosheets with a uniform thickness and a grain size of $\approx 20\ \mu\text{m}$ were obtained. Upon extending the growth time from 10 to 30 min, large-area continuous Cr_5Te_8 films were also obtained on the mica substrate (**Figure S1a**, Supporting Information). X-ray diffraction (XRD) measurements were performed to identify their crystal structure (**Figure S1b**, Supporting Information), wherein the prominent diffraction peaks well match the standard CIF card (CIF No. 1213750) of the Cr_5Te_8 crystal. Rietveld refinement of the XRD using a GSAS+EXPGUI suite confirmed that the Cr_5Te_8 samples crystallized in the trigonal crystal structure with the space group $\text{p}\bar{3}\text{m1}$ and the lattice constants were estimated to be $a = b = 7.90140(9)\ \text{\AA}$ and $c = 6.03850(8)\ \text{\AA}$ (**Table S1**, Supporting Information). X-ray photoelectron spectroscopy (XPS) was used to examine the bonding type and elemental composition of the CVD-grown Cr_5Te_8 . As shown in **Figure 1c**, the peaks located at binding energies of ≈ 576.2 and $586.5\ \text{eV}$ are attributed to Cr $2\text{p}_{3/2}$ and Cr $2\text{p}_{1/2}$, and the peaks located at ≈ 572.2 and $582.5\ \text{eV}$ are attributed to Te $3\text{d}_{5/2}$ and Te $3\text{d}_{3/2}$, respectively. XPS quantitative analysis (peak intensity and binding energy) demonstrates a Cr/Te atomic ratio of $\approx 1:1.62$ with Cr and Te in the $\text{Cr}^{3.2+}$ state and Te^{2-} state (referred to the standard data from handbook of XPS), respectively, consistent well with the stoichiometric ratio of the Cr_5Te_8 crystal. The composition of Cr_5Te_8 was also confirmed by energy-dispersive spectroscopy (EDS) measurements (**Figure S1c**, Supporting Information). Raman spectra of the Cr_5Te_8 nanosheets (**Figure 1e**) show two primary characteristic peaks at 124 and $142\ \text{cm}^{-1}$, corresponding to the out-of-plane A_{1g} and in-plane E_g vibration modes, respectively. Furthermore, Raman intensity mapping images of A_{1g} and E_g modes display the highly uniform thickness and phase structure of Cr_5Te_8 nanosheets. In addition to the mica substrate, we also explored the growth of Cr_5Te_8 on SiO_2/Si (300 nm) and c-cut sapphire substrates, but only many small thick flakes or

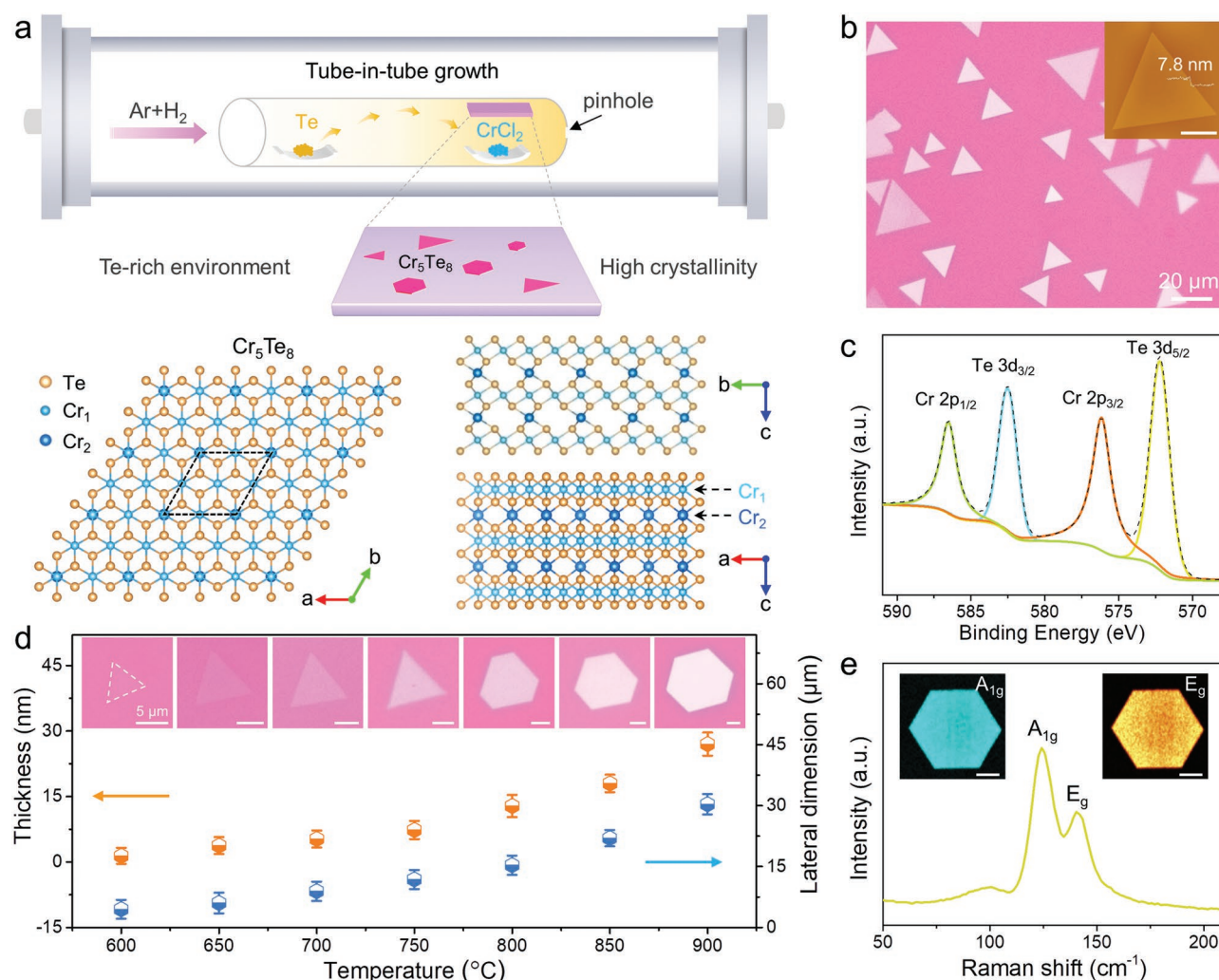


Figure 1. Structural features and synthesis strategy of Cr_5Te_8 . a) Schematic diagram of the tube-in-tube CVD growth approach for the synthesis of Cr_5Te_8 nanosheets and atomic structure (top and side views) of Cr_5Te_8 crystal. b) OM image of as-grown Cr_5Te_8 nanosheets on a mica substrate. Inset is the corresponding atomic force microscopy image. c) XPS of as-grown Cr_5Te_8 nanosheets. d) Statistical thickness and lateral dimension of Cr_5Te_8 nanosheets synthesized at different temperatures. Insets are the corresponding typical OM images. e) Raman spectra of as-grown Cr_5Te_8 nanosheets. Insets are the Raman intensity mapping images of the E_g and A_{1g} modes. All scale bars are 5 μm .

dots were acquired (Figure S2, Supporting Information). The results indicate that the atomically flat mica surface with a lower migration barrier is critical to the successful epitaxy of such nonlayered Cr_5Te_8 crystals down to the 2D limit. We then explored the controllable synthesis of Cr_5Te_8 by modulating the growth temperature from 600 to 900 $^{\circ}\text{C}$, as shown in Figure S3 (Supporting Information). The typical OM images of as-grown Cr_5Te_8 nanosheets on mica and the statistical results (Figure 1d) display a systematic evolution of the thickness (from ≈ 1.2 to ≈ 26 nm), lateral dimension (from ≈ 5 to ≈ 30 μm) and even morphology (from triangle to hexagon) with an increasing growth temperature. Moreover, both Raman intensity and frequency features of Cr_5Te_8 nanosheets show strong thickness dependence (Figure S3i,j, Supporting Information), which can be used to identify the thickness of CVD-grown Cr_5Te_8 nanosheets.

Here, we would like to highlight the importance of the tube-in-tube growth approach for the synthesis of high crystallinity Cr_5Te_8 ultrathin crystals with an accurate composition. The

large above hull energy (0.361 eV/atom) of the Cr_5Te_8 crystal makes it naturally thermally unstable,^[35] which means that it easily decomposes at high temperature. In particular, the conventional CVD growth approach cannot sufficiently, uniformly and persistently supply Te precursor species because of the significant vapor concentration drop during the growth process. The above two factors thermodynamically favor the decomposition of as-synthesized Cr_5Te_8 nanosheets, as shown in Figure S4a–c (Supporting Information), where a quite rough and inhomogeneous sample surface can be clearly observed. Further XPS analysis (Figure S4d, Supporting Information) shows a Cr:Te element ratio of 3.99:1, which is far from that of the Cr_5Te_8 crystal, suggesting the formation of abundant Te vacancies in the as-grown sample. Notably, the decomposition problem of Cr_5Te_8 synthesized with the conventional CVD approach still exists even under Te amounts up to 800 mg (Figure S5, Supporting Information). In contrast, the tube-in-tube growth approach can provide a Te-rich environment

during the entire growth process, which is beneficial to suppress the equilibrium shift to the decomposition direction and facilitate that to the synthesis reaction direction. As a result, high-quality Cr_5Te_8 nanosheets with an accurate stoichiometric ratio and fairly smooth and clean surfaces were obtained, as confirmed by XPS, OM, and atomic force microscopy characterizations (Figure S4f–h, Supporting Information). Notably, using the tube-in-tube growth approach, we can even controllably modulate the composition of Cr_xTe_y (obtaining Cr_3Te_4 , Cr_5Te_8 , and CrTe_2) by tuning the ratio of Cr and Te precursors (Figure S6, Supporting Information). This growth approach provides a new paradigm in synthesizing thermally unstable 2D materials and can be readily extended to a variety of magnetic materials. Furthermore, we also evaluated the air stability of CVD-grown Cr_5Te_8 nanosheets by continuously tracking their structure and surface feature variation for eight months of aging in ambient air. Obviously, the Raman spectra and atomic force microscopy images (Figure S4j, Supporting Information) of the Cr_5Te_8 nanosheets were well maintained for such a long time, indicating an excellent air stability, which is quite important for fundamental property research and practical device applications.

The composition and crystal structure of Cr_5Te_8 nanosheets were further confirmed using EDS and annular dark field aberration-corrected scanning transmission electron microscopy (ADF-STEM). The low-magnification STEM image (Figure 2a) of a hexagonal Cr_5Te_8 nanosheet and the corresponding EDS elemental mapping images (Figure 2b–d) demonstrate the homogeneous spatial distribution of Cr and Te elements throughout the entire sample. Figure 2e shows a typical atomic-resolution ADF-STEM image of the Cr_5Te_8 nanosheet, where the Cr and Te atoms correspond to dark and bright spots due to their small and large atomic numbers (Z). We can observe a nearly perfect periodic atomic arrangement with clearly resolved lattice spacing of 0.200 and 0.201 nm corresponding to the (300) and (3–30) planes of the Cr_5Te_8 crystal, respectively. Obviously, the Cr_5Te_8 nanosheet has a hexagonal 1T phase structure with each hexagonally arranged Cr atom surrounded by six Te atoms, which can be intuitively seen from the corresponding structural model (Figure 2f). Furthermore, the uniform atomic arrangement and almost absence of local discontinuities or defects in the STEM image verify the high crystal quality of the CVD-grown Cr_5Te_8 nanosheets.

As demonstrated above, Cr_xTe_y are a large material family including CrTe_2 , Cr_5Te_8 , Cr_3Te_4 , and CrTe , which can be viewed as the self-intercalation compounds of layered CrTe_2 , and thus, they have quite similar structural features. Moreover, there are two types of thermodynamically stable phases for Cr_5Te_8 crystals: the trigonal phase (t-phase) and the monoclinic phase (m-phase).^[36,37] Hence, distinguishing these degenerate structures and phases, while challenging, was realized by combining quantitative STEM and selected area electron diffraction (SAED) analysis as well as structure simulation (Figure 2h–k). From the two STEM images of the experiment (Figure 2h) and simulation (Figure 2j) of the Cr_5Te_8 crystal, we can see that the intensity and arrangement of each Cr and Te atom are approximately the same. Notably, the contrast of intercalated Cr_2 sites can be distinguished in the simulated STEM image but cannot be distinguished in the experimental STEM image, which

is reasonable because of the much smaller Z of the Cr atom compared with the Te atom and the relatively low energy resolution of our transmission electron microscopy (TEM) equipment. The intensity profiles (Figure 2g) extracted from the experimental and simulated STEM images of Cr_5Te_8 along the yellow dashed lines in Figure 2h,j are consistent in terms of the lattice spacing, indicating a strong match of the atomic structure between our sample and the Cr_5Te_8 crystal. Moreover, the SAED patterns obtained from both the experiment (Figure 2i) and the simulation (Figure 2k) show the same single set of hexagonally arranged diffraction spots, suggesting that the Cr_5Te_8 nanosheet is a single crystal with a hexagonal structure. Notably, the experimental STEM images and SAED patterns of our samples are completely distinct from those of the simulated results of Cr_xTe_y with other possible compositions (Figures S7 and S8 and Table S2, Supporting Information). Furthermore, by comparing the experimental SAED patterns with those of simulated t-phase and m-phase Cr_5Te_8 crystals (Figure S8, Supporting Information), we also confirmed the t-phase structure of the CVD-grown Cr_5Te_8 nanosheets. The STEM results together with the aforementioned XPS and XRD results strongly confirm the composition and phase structure of the CVD-grown Cr_5Te_8 nanosheets. Moreover, high-resolution ADF-STEM and EDS spectra analyses of Cr_5Te_8 samples with different morphologies (such as triangles and truncated triangles) confirm their consistent atomic structure and composition (Figure S9, Supporting Information).

Second harmonic generation (SHG) was used to identify more structural information of the Cr_5Te_8 crystal due to the high sensitivity of this method to the crystal symmetry and orientation and layer-stacking mode of materials.^[9,38] Figure 3a displays a schematic diagram of the SHG measurement process under excitation by a femtosecond laser. SHG signals were generated on the surface of Cr_5Te_8 using light sources of different wavelengths (Figure 3b), showing nonlinear optical characteristics over a wide spectral range of 780–1020 nm. The response spectra observed in the range of 390–510 nm are attributed to the frequency doubling of the excitation wavelength. The strongest SHG response is located at ≈ 900 nm, which was selected for the following SHG exploration. The intensity of SHG signal increases with increasing laser power (Figure 3c), exhibiting a parabolic-like relationship ($I \propto P^\theta$, $\theta = 2.00 \pm 0.06$), as shown in Figure 3d. This result consists well with the electric dipole theory under the first-order perturbation ($I_{\text{SHG}} = |E(2\omega)|^2 \propto |P(\omega)|^2$, where I_{SHG} is the SHG intensity, $E(2\omega)$ is the SHG electric field vector, and $P(\omega)$ is the excitation laser power),^[38] indicating the broken symmetry of Cr_5Te_8 .^[39] Moreover, SHG mapping (Figure 3e) of a hexagonal Cr_5Te_8 nanosheet shows a uniform SHG response throughout the entire sample, verifying the highly pure phase structure. Notably, polarized SHG, which has crystal symmetry dependence, is a powerful tool for studying the angle-resolved structural symmetry. The SHG intensity displays a sixfold rotational symmetry (Figure 3f), and it reaches the maximum value in the zigzag direction. The polarized SHG signal can be well fitted with the equation $I = I_0 \cos^2 3\theta$, where I_0 is the maximum value of the SHG intensity and θ is defined as the azimuthal angle between the direction of excitation field and the mirror plane of the crystal, which suggests the typical hexagonal symmetric feature of the Cr_5Te_8 crystal.

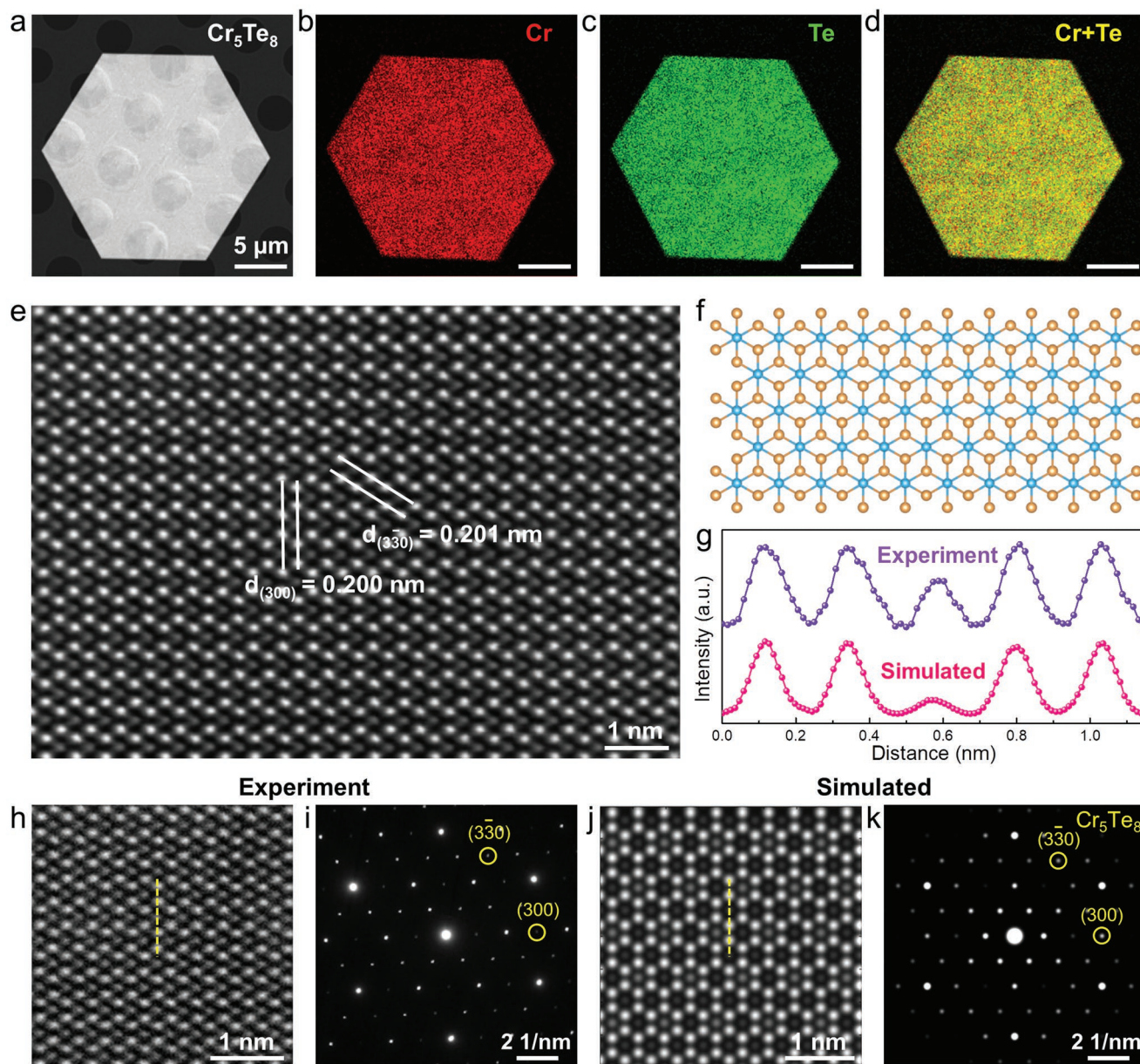


Figure 2. Composition and structural characterization of CVD-grown Cr_5Te_8 nanosheets. a) Low-magnification ADF-STEM image of a few-layer hexagonal Cr_5Te_8 grain. b–d) EDS mapping of Cr (b), Te (c), and an overlay of Cr and Te elements (d) of the Cr_5Te_8 grain. e) High-resolution ADF-STEM image of the Cr_5Te_8 grain and f) corresponding atomic model of the Cr_5Te_8 crystal. g) Intensity profile of experimental (purple curve) and simulated (pink curve) Cr_5Te_8 STEM images along the yellow dashed lines in (h) and (j), respectively. h,i) Experimentally measured ADF-STEM image (h) and SAED pattern (i) of the Cr_5Te_8 crystal. j,k) Simulated ADF-STEM image (j) and SAED pattern (k) of the Cr_5Te_8 crystal.

The successful vdW epitaxial growth of Cr_5Te_8 nanosheets with tunable thickness allows us to systematically explore their thickness-dependent magnetic properties. We examined the magnetic order through MOKE measurements, where a normally irradiated polarized laser was used to detect the MOKE signals of the samples, as schematically shown in Figure S10 (Supporting Information). **Figure 4a** shows the Kerr rotation (θ_K) as a function of the magnetic field for a 15 nm Cr_5Te_8 nanosheet at different temperatures. The obvious magnetic hysteresis loop with a sharp switching edge (the ratio of coercive field H_C to the saturation field H_S (H_C/H_S) was almost

equal to 1) demonstrates that the Cr_5Te_8 nanosheet possesses FM ordering with strong out-of-plane spin polarization.^[11,40] As the temperature increases from 10 to 150 K, the hysteresis loop gradually decreases and finally disappears at a T_C of 130 K. The quantitative analysis of the magnetic anisotropy of Cr_5Te_8 nanosheet would be achieved via the superconducting quantum interference device (SQUID) technique in our future research work.

To reveal the evolution of FM properties of the Cr_5Te_8 crystals from bulk to 2D limit, the temperature dependence of MOKE signals was measured for samples with different thicknesses

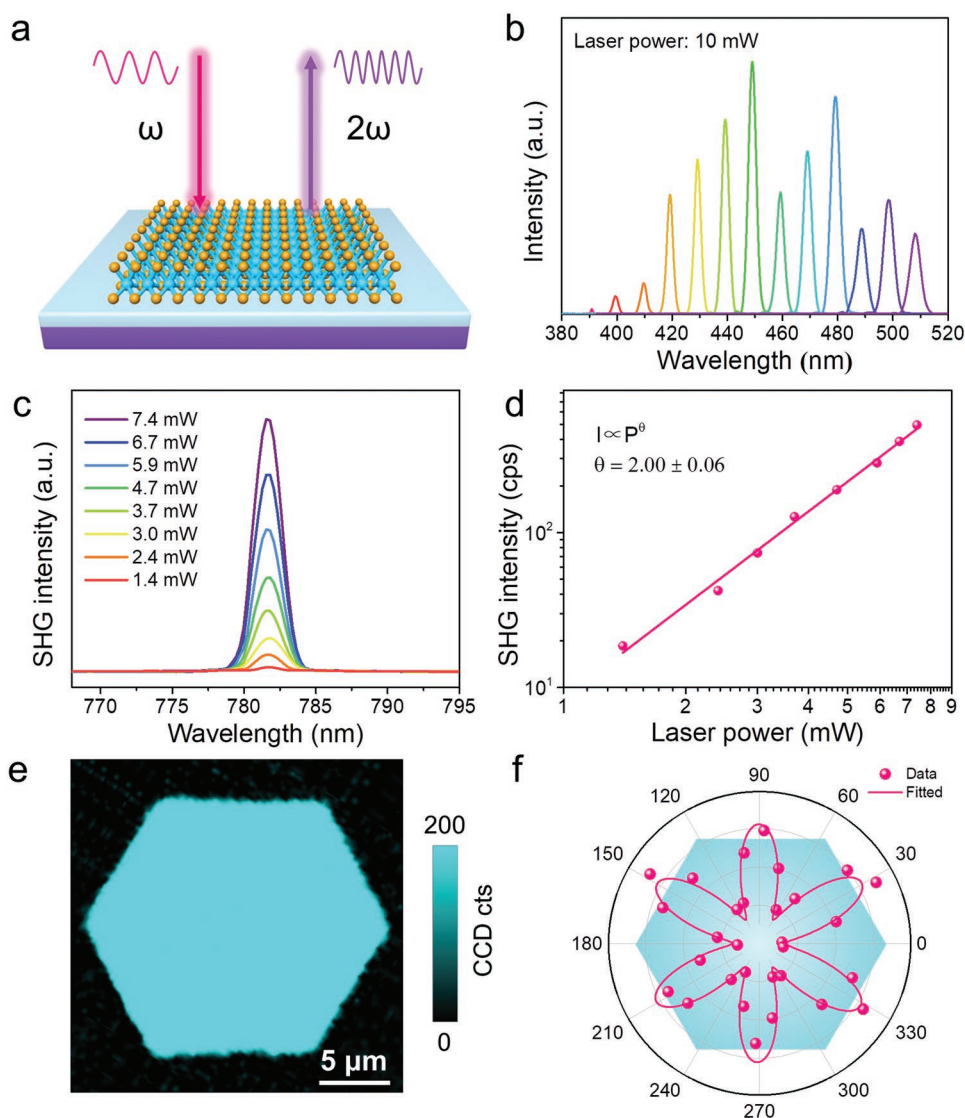


Figure 3. SHG characterization of CVD-grown Cr_5Te_8 nanosheets. a) Schematic diagram of the SHG measurement. b) SHG signals of a Cr_5Te_8 nanosheet measured under different excitation wavelengths. c) Power-dependent SHG spectra of t-phase Cr_5Te_8 nanosheets under a 1550 nm laser. d) SHG intensity as a function of laser power. e) SHG intensity mapping of an individual hexagonal Cr_5Te_8 nanosheet. f) Polarization angle-dependent SHG intensity of Cr_5Te_8 nanosheets with sixfold rotational symmetry.

(Figure S11, Supporting Information). Figure 4b shows θ_K as a function of the magnetic field for the Cr_5Te_8 nanosheets with several typical thicknesses (10, 17, 23, and 30 nm) measured at 50 K. All the four samples display rectangular hysteresis loops, which indicates that the hard magnetic characteristics of Cr_5Te_8 were sustained well when the sample thickness decreased to 10 nm. As shown in Figure 4c, the coercive field (H_C) values extracted from the hysteresis loops of Cr_5Te_8 nanosheets decrease with the sample thickness decreasing. Moreover, the θ_K as a function of temperature for above four Cr_5Te_8 nanosheets exhibits the standard FM temperature dependence (Figure 4d). For each sample, θ_K first slowly decreases with increasing temperature and then rapidly decreases when the temperature approaches T_C . Based on the MOKE data at different temperatures, the magnetic phase diagram of the layer number versus the temperature can be achieved for the CVD-grown Cr_5Te_8

nanosheets (Figure 4e). The resulting phase diagram shows that the FM order is preserved down to 5 nm with a T_C of 50 K, and T_C gradually increases with increasing sample thickness, reaching the value of 160 K at the thickness of 30 nm. Note that such T_C value is still lower than that of Cr_5Te_8 bulk crystal (230 K) reported previously,^[32] which may result from many reasons, such as the limited sample thickness, the dielectric environment variation, the existence of domains wall and the laser heating during MOKE measurement, etc.^[29] We believe that the T_C of CVD-grown 2D Cr_5Te_8 nanosheets would be further enhanced via optimize the above parameters. What's more, the MOKE signals of CVD-grown Cr_5Te_8 nanosheets are well maintained after aging in air for three months (Figure S12, Supporting Information), indicating that Cr_5Te_8 is an air-stable 2D FM material.

Density functional theory (DFT) calculations were performed to provide further insights on the origin of magnetic order.

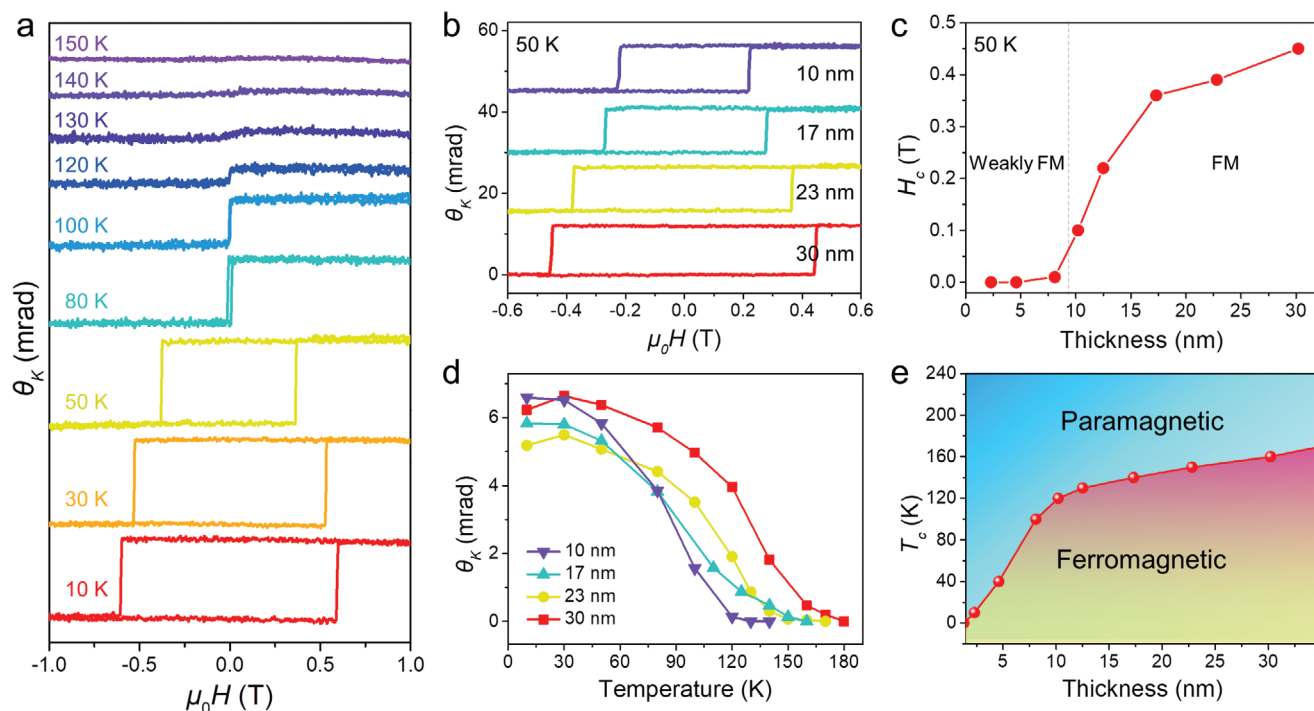


Figure 4. MOKE measurements of Cr_5Te_8 single crystals. a) Hysteresis loops at different temperatures (10–150 K) obtained from a Cr_5Te_8 nanosheet with a thickness of 15 nm. b) Hysteresis loops of Cr_5Te_8 nanosheets with thicknesses of 10, 17, 23, and 30 nm measured at 50 K. c) H_C as a function of thickness. d) θ_K as a function of temperature for the four Cr_5Te_8 nanosheets. e) Thickness-temperature phase diagram of Cr_5Te_8 single crystals.

To facilitate understanding, we used the layer number to depict the thickness of Cr_5Te_8 crystal (Figure S13, Supporting Information) as it can be regarded as the self-intercalated layered 2D material. Our calculation results indicate that the intralayer FM state is energetically preferential in monolayer Cr_5Te_8 with an energy gain of 82.8 meV/Cr compared with the antiferromagnetic (AFM) state (Figure 5a,b), which is attributed to the dominant FM superexchange coupling between magnetic Cr atoms via Te p orbitals. In the case of multilayer Cr_5Te_8 , we only studied the interlayer magnetic coupling due to the nature of intralayer FM coupling as demonstrated above. The spin densities of FM and AFM configurations (Figure 5c,d) in bilayer Cr_5Te_8 show that the interlayer region is filled with the spin-down electrons in FM configuration and the complex of spin-up and spin-down electrons in AFM configuration. This suggests that the Pauli repulsion of the former is larger than that of the latter, which contributes to the interlayer AFM ground state in bilayer Cr_5Te_8 . However, the advantage of interlayer AFM over FM is reduced as the layer number further increases and even inverted when the number of layers reaches seven with the on-site Coulomb potential (U) value of 4 eV (Figure 5e), which is consistent with our experimental observation on multilayer Cr_5Te_8 .

Such an unusual transition between interlayer AFM and FM can be explained by the competition between the Pauli repulsion and the kinetic energy gain across the layers.^[21,41] In the case of few-layer Cr_5Te_8 , the Pauli repulsion is stronger than the kinetic energy gain, thus the AFM configuration is preferred. As the number of layer increases, the energy splitting of interlayer sub-band near the Fermi level (Figure 5f,g) becomes large,

indicating the electrons filling in the sub-band gain a larger kinetic energy. When the kinetic energy gain overcomes the interlayer Pauli repulsion, the interlayer FM coupling will dominate, and thus give rise to robust FM order in thicker Cr_5Te_8 , as proved by the experiment studies. To prove our speculation, we further calculated the U -dependent energy difference between AFM and FM configurations as the increase of U will enhance the Pauli repulsion and reduce the kinetic energy gain. As shown in Figure 5e, the critical number of layer for the transition between AFM and FM states increases with the U increasing, which is in agreement with our deduction.

3. Conclusion

We have successfully synthesized high-quality 2D Cr_5Te_8 nanosheets on mica substrate via a tube-in-tube CVD approach. This new growth strategy provides a Te-rich growth atmosphere, which is critical to the synthesis of high-crystallinity Cr_5Te_8 crystals. By precisely tuning the growth temperature, the thickness of Cr_5Te_8 nanosheets was continuously modulated from 1.2 to 30 nm, with the morphology changing from triangle to hexagon. Extensive STEM characterizations combined with structural simulations confirmed the composition, t-phase structure and high crystallinity of the as-grown Cr_5Te_8 nanosheets. Furthermore, the CVD-grown Cr_5Te_8 nanosheets exhibit an obvious FM property, with a T_C of up to 160 K. More importantly, the Cr_5Te_8 nanosheets exhibit an outstanding air stability, and their MOKE signal remains unchanged after three months of aging in air. The controllable synthesis of Cr_5Te_8

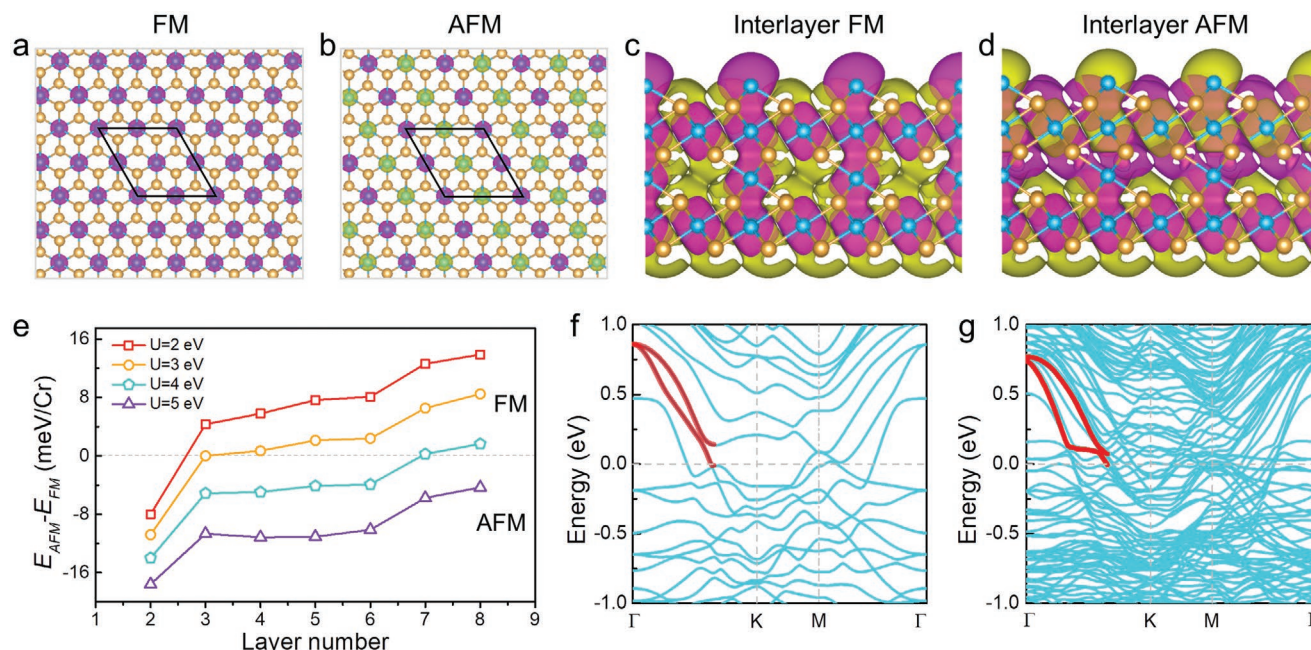


Figure 5. Theory calculations of the magnetism in Cr_5Te_8 . a,b) Spin densities of monolayer Cr_5Te_8 in FM and AFM states with an isosurface value of $0.005 \text{ e Bohr}^{-3}$. The purple and green isosurface contours represent spin-up and spin-down, respectively. c,d) The spin density of bilayer Cr_5Te_8 for interlayer FM and AFM, respectively, where the isosurface value is $0.0005 \text{ e Bohr}^{-3}$. e) AFM–FM energy difference evolution as a function of layer number with different on site U values. f,g) The band structures of 2L- Cr_5Te_8 (f) and 8L- Cr_5Te_8 (g). The Fermi level is set to zero. The red line indicates the range of split interlayer sub-bands in the multilayer Cr_5Te_8 .

together with its outstanding and air-stable FM property opens up new prospects for the study of 2D magnetism and spintronic device applications.

4. Experimental Section

Growth and Transfer of Cr_5Te_8 Nanosheets: High-quality Cr_5Te_8 nanosheets were grown on freshly cleaved mica substrate by tube-in-tube CVD growth. Briefly, Te powder (200–800 mg, Alfa, 99.999%) and CrCl_2 powder (5 mg, Aladdin, 99.9%) were used as Te and Cr precursors, respectively. The Te powder was placed in a quartz boat located at upstream of the hot zone, where the temperature was $\approx 500^\circ\text{C}$. A mica substrate was placed on a quartz boat containing the CrCl_2 source in a face-down configuration at the heating center of the tube furnace. Before the heating process, high-purity argon (Ar, 300 sccm) gas was loaded to purge the reaction chamber for 10 min. Then, the furnace temperature was ramped to the growth temperature ($600\text{--}900^\circ\text{C}$), with a mixture of 50 sccm Ar and 20 sccm hydrogen (H_2) as the carrier gas, and maintained at these temperatures for 10 min to grow Cr_5Te_8 nanosheets. The as-synthesized Cr_5Te_8 nanosheets were transferred onto the target substrate (such as SiO_2/Si (300 nm) substrate and copper grid) via a hydrofluoric acid (HF)-assisted wet transfer approach for further structure and property characterization.

Structure and Composition Characterization: The morphology, phase structure, and thickness of CVD-grown Cr_5Te_8 nanosheets were characterized by OM (BX51, Olympus), XRD (Smart Lab(9)), and atomic force microscopy (Bruker ICON microscope). Raman spectra and mapping images were obtained on a Witec Raman spectroscopy, with excitation of a 532 nm laser. SHG measurements were performed on a homemade optical system with a femtosecond laser (Verdi, Coherent) as the excitation source. The elemental composition of Cr_5Te_8 nanosheets was analyzed by XPS (ESCALAB Xi+). The atomic structure and element

distribution of Cr_5Te_8 were evaluated via high-angle ADF-STEM imaging and EDS mapping on a probe aberration-corrected TEM (Thermo Fisher Titan cubed Themis G2 300) at 300 kV.

Magnetic Property Measurements: MOKE measurements were carried out using a homemade microscopic polar MOKE system. The Cr_5Te_8 samples were placed in a superconducting magnet (Oxford Instruments) with a temperature ranging from 10 to 300 K and an out-of-plane magnetic field up to 5 T. The wavelength of the light source ranged from 540 to 740 nm, with an excitation power of 25 mW. A mechanical chopper and a photoelastic modulator were used to modulate the intensity and polarization of incident light, respectively. The signal was collected by a preamplified photodetector connected to three lock-in amplifiers.

Density Functional Theory Calculations: First-principles calculations were carried out within the framework of DFT as implemented in the Vienna Ab initio Simulation Package (VASP).^[42,43] The pseudopotentials was treated by projector augmented-wave (PAW) method^[44] with a cutoff energy of 400 eV for plane-wave expansion. The electron exchange correlation potential was described by the generalized gradient approximation (GGA) with Perdew–Burke–Ernzerhof (PBE) parameterization.^[45] To describe the strong-correlation effects in Cr atom, on-site Coulomb interaction was introduced using Dudarev's GGA+ U approach with U value of 4 eV.^[46] The impact of U value on interlayer magnetic coupling was studied via tuning U value from 2 to 5 eV. The atomic positions were fully optimized with a conjugate gradient algorithm until the Hellman-Feynman force on each atom are less than 0.01 eV \AA^{-1} . To avoid interactions between the adjacent periodic images, a vacuum space of 18 Å was set.

Supporting Information

Supporting Information is available from the Wiley Online Library or from the author.

Acknowledgements

C.C., X.C., and C.W. contributed equally to this work. This work was supported by the National Natural Science Foundation of China (51972204, 22003074, 21825103), the Natural Science Basic Research Plan in Shaanxi Province (2018JQ5192), the Science and Technology Program of Shaanxi Province (2017KJXX-16), the Fundamental Research Funds for the Central Universities in Shaanxi Normal University (GK201802003), the State Key Laboratory of Mechanics and Control of Mechanical Structures (Nanjing University of Aeronautics and astronautics) (MCMS-E-0420G01), and SIAT Innovation Program for Excellent Young Researchers, the Guangdong Basic and Applied Basic Research Foundation (2020A1515110580). The authors acknowledge the help of Qi Li from Shaanxi Normal University and Longhai Yang from Xi'an University of Science and Technology for the XRD refinement.

Conflict of Interest

The authors declare no conflict of interest.

Data Availability Statement

Research data are not shared.

Keywords

2D materials, Cr₅Te₈, CVD growth, ferromagnetism, tunable thickness

Received: September 20, 2021
Published online: November 12, 2021

- [1] S. Manzeli, D. Ovchinnikov, D. Pasquier, O. V. Yazyev, A. Kis, *Nat. Rev. Mater.* **2017**, 2, 17033.
- [2] Z. Y. Cai, B. L. Liu, X. L. Zou, H.-M. Cheng, *Chem. Rev.* **2018**, 118, 6091.
- [3] K. S. Novoselov, A. Mishchenko, A. Carvalho, A. H. Castro Neto, *Science* **2016**, 353, aac9439.
- [4] X. B. Li, C. Chen, Y. Yang, Z. B. Lei, H. Xu, *Adv. Sci.* **2020**, 7, 2002320.
- [5] M. Gibertini, M. Koperski, A. F. Morpurgo, K. S. Novoselov, *Nat. Nanotechnol.* **2019**, 14, 408.
- [6] D. J. O'Hara, T. C. Zhu, A. H. Trout, A. S. Ahmed, Y. K. Luo, C. H. Lee, M. R. Brenner, S. Rajan, J. A. Gupta, D. W. McComb, R. K. Kawakami, *Nano Lett.* **2018**, 18, 3125.
- [7] C. Gong, X. Zhang, *Science* **2019**, 363, eaav4450.
- [8] Y. Khan, S. M. Obaidulla, M. R. Habib, A. Gayen, T. Liang, X. F. Wang, M. S. Xu, *Nano Today* **2020**, 34, 100902.
- [9] Z. Y. Sun, Y. F. Yi, T. C. Song, G. Clark, B. Huang, Y. W. Shan, S. Wu, D. Huang, C. L. Gao, Z. H. Chen, M. McGuire, T. Cao, D. Xiao, W.-T. Liu, W. Yao, X. X. Xu, S. W. Wu, *Nature* **2019**, 572, 497.
- [10] S. W. Jiang, L. Z. Li, Z. f. Wang, K. F. Mak, J. Shan, *Nat. Nanotechnol.* **2018**, 13, 549.
- [11] B. Huang, G. Clark, E. Navarro-Moratalla, D. R. Klein, R. Cheng, K. L. Seyler, D. Zhong, E. Schmidgall, M. A. McGuire, D. H. Cobden, W. Yao, D. Xiao, P. Jarillo-Herrero, X. D. Xu, *Nature* **2017**, 546, 270.
- [12] T. Kong, K. Stolze, E. I. Timmons, J. Tao, D. R. Ni, S. Guo, Z. Yang, R. Prozorov, R. J. Cava, *Adv. Mater.* **2019**, 31, 1808074.
- [13] Z. Wang, T. Y. Zhang, M. Ding, B. J. Dong, Y. X. Li, M. L. Chen, X. X. Li, J. Q. Huang, H. W. Wang, X. T. Zhao, Y. Li, D. Li, C. K. Jia, L. D. Sun, H. H. Guo, Y. Ye, D. M. Sun, Y. S. Chen, T. Yang, J. Zhang, S. Ono, Z. Han, Z. D. Zhang, *Nat. Nanotechnol.* **2018**, 13, 554.
- [14] C. Gong, L. Li, Z. L. Li, H. W. Ji, A. Stern, Y. Xia, T. Cao, W. Bao, C. Z. Wang, Y. Wang, Z. Q. Qiu, R. J. Cava, S. G. Louie, J. Xia, X. Zhang, *Nature* **2017**, 546, 265.
- [15] B. Huang, G. Clark, D. R. Klein, D. MacNeill, E. Navarro-Moratalla, K. L. Seyler, N. Wilson, M. A. McGuire, D. H. Cobden, D. Xiao, W. Yao, P. Jarillo-Herrero, X. D. Xu, *Nat. Nanotechnol.* **2018**, 13, 544.
- [16] Y. J. Deng, Y. J. Yu, Y. C. Song, J. Z. Zhang, N. Z. Wang, Z. Y. Sun, Y. F. Yi, Y. Z. Wu, S. W. Wu, J. Y. Zhu, J. Wang, X. H. Chen, Y. B. Zhang, *Nature* **2018**, 563, 94.
- [17] S. H. Lu, Q. H. Zhou, Y. L. Guo, Y. H. Zhang, Y. Wu, J. L. Wang, *Adv. Mater.* **2020**, 32, 2002658.
- [18] L. X. Kang, C. Ye, X. X. Zhao, X. Y. Zhou, J. X. Hu, Q. Li, D. Liu, C. M. Das, J. F. Yang, D. Y. Hu, J. Q. Chen, X. Cao, Y. Zhang, M. Z. Xu, J. Di, D. Tian, P. Song, G. Kutty, Q. S. Zeng, Q. D. Fu, Y. Deng, J. D. Zhou, A. Ariando, F. Miao, G. Hong, Y. Z. Huang, S. J. Pennycook, K.-T. Yong, W. Ji, X. R. Wang, Z. Liu, *Nat. Commun.* **2020**, 11, 3729.
- [19] Y. Zhang, J. W. Chu, L. Yin, T. A. Shifa, Z. Z. Cheng, R. Q. Cheng, F. Wang, Y. Wen, X. Y. Zhan, Z. X. Wang, J. He, *Adv. Mater.* **2019**, 31, 1900056.
- [20] X. G. Wang, C. Bian, Y. X. He, J. Guo, P. Zhang, L. X. Liu, Y. Wei, L. J. Meng, H. N. Jiang, B. X. Li, A. M. Nie, L. H. Bao, Y. J. Gong, *Mater. Today* **2021**, 45, 35.
- [21] B. Li, Z. Wan, C. Wang, P. Chen, B. Huang, X. Cheng, Q. Qian, J. Li, Z. W. Zhang, G. Z. Sun, B. Zhao, H. F. Ma, R. X. Wu, Z. M. Wei, Y. Liu, L. Liao, Y. Ye, Y. Huang, X. D. Xu, X. D. Duan, W. Ji, X. F. Duan, *Nat. Mater.* **2021**, 20, 818.
- [22] M. Bonilla, S. Kolekar, Y. J. Ma, H. C. Diaz, V. Kalappattil, R. Das, T. Eggers, H. R. Gutierrez, M.-H. Phan, M. Batzill, *Nat. Nanotechnol.* **2018**, 13, 289.
- [23] F. F. Cui, X. X. Zhao, J. J. Xu, B. Tang, Q. Y. Shang, J. P. Shi, Y. H. Huan, J. H. Liao, Q. Chen, Y. L. Hou, Q. Zhang, S. J. Pennycook, Y. F. Zhang, *Adv. Mater.* **2020**, 32, 1905896.
- [24] S. S. Zhou, R. Y. Wang, J. B. Han, D. L. Wang, H. Q. Li, L. Gan, T. Y. Zhai, *Adv. Funct. Mater.* **2019**, 29, 1805880.
- [25] J. W. Chu, Y. Zhang, Y. Wen, R. X. Qiao, C. C. Wu, P. He, L. Yin, R. Q. Cheng, F. Wang, Z. X. Wang, J. Xiong, Y. R. Li, J. He, *Nano Lett.* **2019**, 19, 2154.
- [26] X. C. Huang, J. Q. Guan, Z. J. Lin, B. Liu, S. Y. Xing, W. H. Wang, J. D. Guo, *Nano Lett.* **2017**, 17, 4619.
- [27] C. Niu, G. Qiu, Y. Wang, Z. Zhang, M. Si, W. Wu, P. D. Ye, *Phys. Rev. B* **2020**, 101, 205414.
- [28] K. Lasek, P. M. Coelho, K. Zborecki, Y. Xin, S. K. Kolekar, J. F. Li, M. Batzill, *ACS Nano* **2020**, 14, 8473.
- [29] L. J. Meng, Z. Zhou, M. Q. Xu, S. Q. Yang, K. P. Si, L. X. Liu, X. G. Wang, H. N. Jiang, B. X. Li, P. X. Qin, P. Zhang, J. L. Wang, Z. Q. Liu, P. Z. Tang, Y. Ye, W. Zhou, L. H. Bao, H.-J. Gao, Y. J. Gong, *Nat. Commun.* **2021**, 12, 809.
- [30] Y. Wen, Z. H. Liu, Y. Zhang, C. X. Xia, B. X. Zhai, X. H. Zhang, G. H. Zhai, C. Shen, P. He, R. Q. Cheng, L. Yin, Y. Y. Yao, M. G. Sendeku, Z. X. Wang, X. B. Ye, C. S. Liu, C. Jiang, C. X. Shan, Y. W. Long, J. He, *Nano Lett.* **2020**, 20, 3130.
- [31] M. S. Wang, L. X. Kang, J. W. Su, L. M. Zhang, H. W. Dai, H. Cheng, X. T. Han, T. Y. Zhai, Z. Liu, J. B. Han, *Nanoscale* **2020**, 12, 16427.
- [32] Y. Liu, M. Abeykoon, E. Stavitski, K. Attenkofer, C. Petrovic, *Phys. Rev. B* **2019**, 100, 245114.
- [33] X. Zhang, T. L. Yu, Q. Y. Xue, M. Lei, R. Z. Jiao, *J. Alloys Compd.* **2018**, 750, 798.
- [34] M. Li, Z. W. Ma, J. Yan, C. X. Liu, X. Luo, Y. P. Sun, Q. C. Liu, Z. G. Sheng, *Appl. Phys. Lett.* **2020**, 117, 232404.
- [35] A. Jain, S. P. Ong, G. Hautier, W. Chen, W. D. Richards, S. Dacek, S. Cholia, D. Gunter, D. Skinner, G. Ceder, K. A. Persson, *APL Mater.* **2013**, 1, 011002.
- [36] Y. Liu, C. Petrovic, *Phys. Rev. B* **2018**, 98, 195122.

- [37] Z.-L. Huang, W. Kockelmann, M. Telling, W. Bensch, *Solid-State Sci.* **2008**, *10*, 1099.
- [38] J. W. Su, M. S. Wang, Y. Li, F. K. Wang, Q. Chen, P. Luo, J. B. Han, S. Wang, H. Q. Li, T. Y. Zhai, *Adv. Funct. Mater.* **2020**, *30*, 2000240.
- [39] X. Zhou, J. X. Cheng, Y. B. Zhou, T. Cao, H. Hong, Z. M. Liao, S. W. Wu, H. L. Peng, K. H. Liu, D. P. Yu, *J. Am. Chem. Soc.* **2015**, *137*, 7994.
- [40] J. W. Su, M. S. Wang, G. H. Liu, H. Q. Li, J. B. Han, T. Y. Zhai, *Adv. Sci.* **2020**, *7*, 2001722.
- [41] C. Wang, X. Y. Zhou, L. W. Zhou, Y. H. Pan, Z.-Y. Lu, X. G. Wan, X. Q. Wang, W. Ji, *Phys. Rev. B* **2020**, *102*, 020402.
- [42] G. Kresse, J. Hafner, *Phys. Rev. B* **1993**, *48*, 13115.
- [43] G. Kresse, J. Furthmüller, *Phys. Rev. B* **1996**, *54*, 11169.
- [44] P. E. Blöchl, *Phys. Rev. B* **1994**, *50*, 17953.
- [45] J. P. Perdew, K. Burke, M. Ernzerhof, *Phys. Rev. Lett.* **1996**, *77*, 3865.
- [46] S. L. Dudarev, G. A. Botton, S. Y. Savrasov, C. J. Humphreys, A. P. Sutton, *Phys. Rev. B* **1998**, *57*, 1505.